Large-Scale Data-Driven Comparison of Earthshine Model Effectiveness from Photometric Observations of Diverse LEO Satellites

Timothy Olson, Clarice Reid, Russ Johnson
Slingshot Aerospace
Jeff Shaddix, Dylan Kesler, Belinda Marchand
Slingshot Aerospace

ABSTRACT

Reflectance modeling is important for the study of object photometry and development of optical tracking systems. When estimating resident space object (RSO) brightness, it is essential to not only model solar light that is reflected directly off the RSO but also to capture significant contributions from other sources such as solar light reflected off nearby celestial bodies. The contribution of solar light that is reflected off of the Earth's surface onto a nearby RSO is colloquially known as "earthshine". We provide a side-by-side comparison of several existing and novel models which seek to capture the impact of earthshine on predicted RSO brightness and to compare those results to RSO brightness in several illumination conditions with analytic, numerical, and data-driven methods.

1. INTRODUCTION

Since 2010 the number of orbiting resident space objects objects (RSOs) has grown tremendously, with the majority of the RSO population residing in low Earth orbit (LEO) [1]. As a result of this rapid growth, demand for actionable space domain awareness (SDA) continues to grow to enable safety of transit and space sustainability. For instance, SDA data plays a crucial role in identifying risks from known nearby RSOs, assessing threats from debris clouds resulting from breakup events, and troubleshooting anomalous behavior of space-based assets.

Government and commercial space situational awareness sensors support the SDA mission today, proliferated around the globe and leveraging multiple sensing modalities. Optical systems are among the top three sensing modalities supporting the global SDA mission, which additionally include radar and passive radio frequency (RF) tracking sensors. Optical systems specifically deliver both astrometric and photometric data on the objects tracked. Photometric data refers to the apparent brightness of the object within specific wavelength ranges. Astrometric data alludes to precise, high-accuracy angular measurements of the position of the objects being tracked.

As the space object population rises, the demand for space object tracking sensors that can effectively monitor the growing population continues to grow, and optimizing the utilization and scheduling of these systems becomes an increasingly important task. To that end, estimating the predicted brightness of RSOs accurately can play a valuable role in optimizing the tasking of tracking sensors. Apparent brightness, in general, depends on a number of variables and conditions, such as direct solar reflections off the RSO toward a given sensor. Of course, direct solar light is not the only contributing light source [2, 3, 4, 5]. Nearby celestial bodies can also reflect light onto an RSO. For RSOs orbiting near the Earth, the contribution of the solar light reflected from the surface of the Earth back to the RSO is called earthshine.

In this work, we present a comparison between several brightness estimation models for RSOs in LEO, focusing on how earthshine changes model accuracy. Slingshot has gathered large data sets with its LEO optical fence (Horus) and its daytime capable gimbaled system (Varda), which are used to compare the efficacy of the considered models, fit relevant parameters to create data-driven models, and assess the impacts of earthshine across this cathemeral dataset.

2. BACKGROUND AND PRIOR WORK

Since the launch of Sputnik in 1957, there has been abundant interest in understanding and predicting the RSO brightness during remote observation using electro-optical systems [2]. This interest in modeling RSO brightness has grown

commensurately with the number of satellites in orbit, and has given rise to a plethora of brightness models that can be used to estimate RSO brightness for various illumination conditions. While it is beyond the scope of this work to summarize the entirety of RSO brightness models developed in the last seventy years, in this section we briefly summarize some of the early foundational work in RSO brightness estimation and present relevant modern updates.

2.1 Original Satellite Brightness Modeling (no earthshine)

Capturing all physical phenomena relevant to reflectance-based RSO brightness is challenging due to factors such as complex viewing geometries, illumination conditions, and surface reflectance profiles. To reduce the estimation problem into something more tractable, early efforts in RSO brightness estimation simplified the assumed geometric shape of the object to mitigate complexity [2]. Simplified viewing geometries and other approximations regarding surface reflectance characteristics yielded compact closed-form formulas for estimating the solar reflectance fraction [2] for both specular and diffuse sphere and cylinder-based models. Ref. [2] derived the now ubiquitous formula for computing the relative fraction of incident flux from a distant constant illumination source reflected off of a diffuse sphere toward an observer:

$$F(a,r,\Phi) = \frac{2ar^2}{3\pi d^2}\left(\sin(\Phi) + (\pi - \Phi)\cos(\Phi)\right), \tag{1}$$

where a is the surface albedo of the sphere, r is the radius of the sphere, d is the distance between the center of the sphere and the observer, and Φ is the angle between the to-source and to-observer vectors from the sphere's center. Other models are presented in [2], however the simplicity of (1) and relative ease of computation has made this model a lasting baseline against which new models are measured [6, 7].

Though the diffuse sphere reflectance model has proven to be useful for many applications, due to its simplicity it does not capture all relevant reflective phenomenon. Indeed, several studies have been conducted in which observed RSO brightness has been compared with predicted magnitudes, see [6, 7, 8] for a few such references. In response to this, new models have been developed to capture additional complexities.

2.2 GEO Analyses

Several models have been developed to improve upon the predictive power of (1) for RSOs in geosynchronous orbit (GEO). In, for example, [3] it was shown empirically that the observed brightness of RSOs in GEO did not diminish proportionally to the reduction predicted in the (1) for a large phase angle ($\Phi > 100^\circ$). Thus, several models have been adapted to increase the predictive power of the RSO brightness models. In [3], it is still assumed that the target is a diffuse sphere, however the constant albedo a in (1) is replaced with a piecewise polynomial in the phase angle Φ that is fit based on empirical data.

Further work has been done to extend the simple diffuse sphere model and introduce the geometric effects of the solar panels as well as the impacts of earthshine [6].[1] In this treatment, the RSO is still represented as a diffuse sphere. However the solar panels are introduced as diffuse panels with solar facing and anti-solar facing surfaces, each given their own albedo. Each of these components contributes additively to the overall brightness of the target in the brightness estimate. Moreover, this model considers the contribution of earthshine to the overall estimated target brightness by treating the Earth as a secondary illumination source. The Earth is treated as a diffuse sphere, and the relative fraction of the earthshine is computed via (1) where the RSO is treated as the observer. The computations proceed as expected where the Earth's location is the new illumination source and the aforementioned earthshine flux is used as a scaling factor. As seen in [6], the inclusion of earthshine captured well the phenomenon of increased RSO brightness for large phase angles with simple geometric assumptions. A feature in the derivation of (1) is the uniform flux of the illumination sources at the location of the reflecting body. In geosynchronous orbit, the relatively large distance of the RSO from the Earth and relatively small angular subtense of the earth imply that angular variation will be small and the assumption of stability of the light reflected from the Earth is not ill-founded.

2.3 LEO Analyses

For RSOs in LEO, the assumption of uniform illumination from light reflected off of the Earth's surface is not appropriate. An RSO transitioning across the terminator will see the Earth's surface illuminated at one portion of the orbit and dark at another. Representations of earthshine similar to those seen in [6] are not readily applicable to RSOs in LEO, yet earthshine cannot be neglected either.

[1] The reader should note that the summarized content in this work reflects a small correction to the originally published work in [6]. The discrepancies between the summarized model are usage of distance of the center of the earth and the RSO cosine falloff of the earthshine on the back of the solar panel. These corrections were originally pointed out to the authors by [9].

Several models attempt to more robustly capture the contribution of earthshine to the overall brightness of a LEO target [7, 8]. In these works, the Earth's surface is discretized into a number of flat facets as described in [7]. Here, a relatively straightforward approach is presented to in which the various facets are assigned a Phong reflection model and the diffuse component, specular component, and peak sharpness are all fit based on CARs and CLASIC data collected previously for both land and water. While [7] did not conclude that earthshine improved the predictive power of the brightness model, it was noted that there was little earthshine contribution given the viewing conditions for the considered data. In [8, 10] on the other hand, the considered data is restricted to daytime observations of Starlink satellites and it is noted that the contribution of earthshine leads to a strong improvement in predictive power, although a simplified earthshine model was used. Slingshot Aerospace has also generated RSO "fingerprints" from photometric observations [11]. Although earthshine was not explicitly modeled in that analysis, it may be an important implicit contributor to the inferred fingerprints in certain viewing geometries.

3. METHODS

The goal of this project is to employ a large dataset of real world observations to compare the myriad earthshine models with a data-driven approach. We approach the challenge of earthshine model evaluation in two stages: first by generating synthetic photometry with each model to understand and interpret overall model characteristics and trends, and then by comparing specific model predictions with actual photometric observations to assess their applicability to the real world. In this section of the paper, we introduce the data collection and generation methodologies, provide detailed definitions of each included earthshine model family, unpack the representative satellite geometries used in the analysis, and finally introduce our techniques for fitting unknown parameters and evaluating model performance.

3.1 Photometry

Unresolved photometric observations are collected by assimilating incoming photons received from a reflecting body in orbit around Earth; in particular we limit our analysis to optical-wavelength photons collected from RSOs in LEO. The collected photons do not originate from the RSOs (if the RSO produces any self-illumination, it is assumed to be insignificant compared to the total reflected radiation), rather they are principally produced by the Sun and reflect off the body of the satellite before being collected by the sensor. There may be additional reflections off other bodies while en route from the Sun, such as off the Earth or Moon. The dominant sources of illumination are expected to be direct radiation from the Sun, and reflected solar radiation from Earth's surface; as justified in [7], other sources of illumination may be neglected for the purposes of RSO brightness prediction.

The incident photons are reflected from various surfaces of the satellite body according to the bidirectional reflectance distribution function (BRDF) of the reflecting surface. Some fraction of that reflected radiation may be directed toward an observer – for our purposes, assumed to be a ground observer, but the same principle applies to space-based observers as well – where the total flux of collected photons provides a quantitative measure of satellite brightness. To standardize the brightness measurements, observed photometric flux from the RSO, F_{sat}, is converted to an apparent satellite magnitude referenced against non-reflected incident solar flux, F_{sun} according to:

$$m = -2.5(\log_{10}(F_{sat}) - \log_{10}(F_{sun})) . \tag{2}$$

We consider both flux and magnitude representations in our analysis, as described below.

3.2 Real Data Overview

The real-world photometric observations utilized in our analysis were collected by Slingshot Aerospace's global sensor network [12]. The full data set includes over 2 billion observations as of January 2025, collected across multiple sensor locations around the globe; however, to reduce potential confounding effects and ensure relatively consistent geography for earthshine estimations, we limit the data considered in this report to a single observatory site located in Chile. We further limit the time period to work around network maintenance windows and hence include observations collected over a one-month time period from 00UTC 01 January 2025 up to 00UTC 01 February 2025. We select this observatory site because it includes two co-located sensors: a nighttime optical fence, and a gimbaled optical system that leverages Slingshot's daytime tracking technology – both producing astrometric and photometric observations. The former produces a large quantity of observations across all detectable objects that transit within its 360-deg field of view, while the latter produces fewer total observations but enables daytime collects wherein a larger portion of Earth's illuminated surface may be in view of the satellite, which is relevant to the central consideration of this report.

Table 1: Average number of objects seen per bus type per day

Object Bus Type	Daytime Object Count	Nighttime Object Count
ARROW 150	1	422
ELITEBUS (IRIDIUM NEXT)	1	58
LM-700 IRIDIUM	1	19
SSL-400 GLOBALSTAR	0	48
STARLINK v1.0	1	232
STARLINK v1.5	1	1023
STARLINK v2 Mini Std (Bus 9-2)	1	611
STRELA-1M (ZEYA)	2	201

We focus on a subset of observations covering specific constellations and bus types, chosen for their notable differences in orbit, which provide different solar and earthshine illumination geometries. The average number of distinct objects and average number of observations seen during the day and night are broken down by chosen constellations and bus types in Table 1.

The data are split into temporally non-overlapping fit and evaluation periods. We use the first two weeks of the month (Jan 1-16) as training data to fit the model parameters, and then evaluate performance on the unseen remainder of the month (Jan 17-31). Due to the large imbalance between day and night collections, we downsample the nighttime observations so as not to overwhelm the daytime observations in the fits, which were much lower in count.

Collected measurements are processed to generate and update estimated position and velocity states for the observed RSO. We use the state estimates to reconstruct the illumination and observer geometry at the time of observation.

3.3 Synthetic Data Overview

In addition to real observation data, we also consider synthetic observations generated by evaluating a brightness model on a hypothetical satellite at a chosen orbital position and physical body configuration. The synthetic data are especially useful for identifying key sensitivities and differences between models.

We arrange our synthetic scenarios to encompass a variety of interesting viewing geometries by placing the sensor at an equatorial latitude with an angle of φ_i from the sun direction, and simulating multiple orbital and solar positions. For simplicity of presentation, we only report results on a limited set of illumination geometries: a satellite is placed in a circular, equatorial orbit at 500km altitude and another at 40000km altitude with positions sampled at regular intervals from the orbit, and we place the sun at two elevations above the equator (solar latitudes), 0° and 20°. In the illustrative sketch, Fig. 2, the terminator crosses the satellite orbit at $\varphi = 90^\circ$ and 270°.

Finally, we draw a distinction between flux (per unit area) at the satellite, $\tilde{F}$, and flux at the sensor, F. The former represents the incident photometric flux at the reflecting body (satellite), while the latter represents the flux that actually reaches the observer. Since photometric flux from a source to observer scales with the inverse-square of the intervening distance, the range-normalized flux (flux times range-squared) that an observer would receive from a perfect mirror aligned precisely to reflect 100% of sunlight directly to the observer is identical to the flux at the satellite. In other cases, the observer receives a fraction of the incident flux at the satellite, governed by the BRDF of the reflecting surface. Ultimately, one must account for both the BRDF and relative geometry to fully account for the observed flux, but in some cases it will be instructive to consider the (simulated) flux at the satellite, independently of the reflections.

3.4 Reflectance Models of Earth & Satellite

We include two categories of reflecting surfaces: Lambertian, also called diffuse, and specular surfaces. We consider diffuse surfaces separately, as well as a traditional diffuse + specular combination known as a Phong model [13].[2] We represent both with the combined Phong BRDF:

$$\text{BRDF} = \frac{k_d}{\pi} + k_s \frac{n+2}{2\pi} \left(\hat{u} \cdot \hat{R}\right)^n \tag{3}$$

[2]For numerical ease, we do not factor out the cosine of the angle between observer and surface normal vectors; other references may treat this differently. We note that future work on this topic could compare the relative merit of other reflecting surface models, such as the traditional (cosine-scaled) Phong model, Blinn-Phong[14], and more.

where k_d and k_s are coefficients representing the contributions of each component, n is the specular shininess parameter, $\hat{u}$ is a unit vector in the direction of the observer, $\hat{R}$ is a unit vector pointing in the specular direction whose unnormalized vector $\vec{R}$ is computed from the surface normal $\hat{N}$ and source direction $\hat{L}$:

$$\vec{R} = 2(\hat{L} \cdot \hat{N})\hat{N} - \hat{L}. \tag{4}$$

Pure diffuse reflection ($n = 0$) can be modeled by enforcing either $k_s = 0$ or $k_d = 0$ since the terms become redundant.

We treat all elements with the above methodology, including Earth and all satellite reflecting surfaces. Presumably land and water could have different shininess parameters and reflection coefficients, likewise satellite surfaces differ in reflection details as well due to different material compositions. Although we do not treat this in full fidelity, we do consider three distinct shininess values for both Earth and satellite, in addition to pure diffuse reflections. The coefficients k_d and k_s are inferred separately for land, water, and each satellite surface by fitting to real observations.

3.5 Modeled Body Geometries

A typical satellite is composed of multiple components, each of which may contain multiple exterior surfaces that could potentially reflect illumination toward the observer. If a high-quality computer-aided design (CAD) representation of the satellite is available, then an operator could compute the expected reflectance from that model directly. However, in the absence of such information for most objects on orbit, we consider an alternative, data-driven approach that consists of stitching together a collection of representative surfaces whose effective reflectivity is inferred by fitting to real data. The effective reflectivity K is defined as the product of the reflection coefficient, k_d or k_s respectively, times a measure of surface area – we generally use the actual surface area for flat panels, while for spheres we use the square of the radius – the choice of measure affects the overall normalization of the reflectivity. In practice since K is a linear scale factor for each term, we often treat specular and diffuse reflection separately so that we can define a unit effective reflectivity for each as $K \equiv 1$ during model calculations and then fit a linear combination of the specular and diffuse components to obtain data-derived estimates of the respective K values.

The surfaces considered in our analysis include:

1. **Sphere:** a simple isotropic reflecting sphere. In the case of a diffuse reflecting sphere, we are dealing with unresolved imagery at long range, so we can directly compute the approximate reflected flux from the diffuse sphere equation, (1). Specular reflection is handled by breaking the sphere into microfacets, similar to the faceted Earth described below, and summing over the total discrete flux reflected from each microfacet.
2. **Sun-facing plate:** a flat surface representing a sun-tracking solar panel. It has two sides, the normal vector on the sun-facing side is identical to the satellite-to-sun unit vector; the normal vector on the anti-sun side points in the opposite direction. We note that this may not be entirely physically accurate if additional mission or satellite body configuration constraints prevent the solar panels from freely articulating in all three dimensions, nor does it account for intentional off-pointing as is known to be utilized by Starlink v2 satellites [15].
3. **Nadir-facing plate:** a flat surface representing the nadir face, i.e. bottom, of a boxy or panel-shaped satellite bus. It was previously shown that this is a significant source of specular reflection for SpaceX Starlink satellites [7], and in principle could be a contributor on other satellite bodies as well. We therefore allow our data-driven method to fit parameters for both specular and diffuse reflections off a nadir-facing surface.

While other faces of a boxy satellite could also contribute noticeable reflections, modeling those surfaces requires attitude and geometry details that are difficult to approximate in full generality. Furthermore there are relatively limited geometries for which those surfaces are expected to be in view of both sensor and illumination source (e.g. an anti-nadir surface will never be visible from a ground sensor). We therefore exclude other surfaces from consideration.

3.6 Direct Solar Illumination Model

We turn now to the various reflected illumination models. The dominant source of satellite brightness over a wide range of solar phase angles is due to direct reflection of solar illumination off the body or panels of the satellite to the sensor. We can evaluate the solar reflection directly from the following elements (assuming $K \equiv 1$):

1. $\hat{L}$: unit vector pointing from satellite to sun
2. $\hat{u}$: unit vector pointing from satellite to observer
3. $\hat{N}$: unit normal vector of the satellite surface element (not needed for a diffuse sphere component)
4. n_{sat}: satellite shininess parameter (0 for diffuse surface)

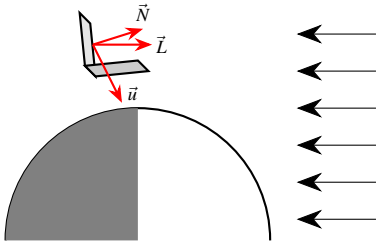

Fig. 1: The solar panel and satellite body contribute to overall brightness estimate by reflecting incident sunlight directly to the observer.

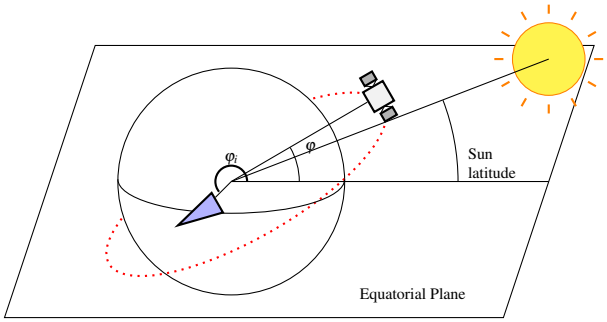

Fig. 2: Example illustration of synthetic data geometry with the equatorial sensor at polar angle φ_0, the satellite positions sampled at multiple points in a representative orbit, and the sun fixed at $\varphi = 0$ with a specified elevation above the equatorial plane.

5. d: range from satellite to sensor

The total reflected solar flux from a flat satellite surface is then proportional to:

$$F_{\text{solar}} \propto \frac{n_{\text{sat}} + 2}{2\pi d^2} \left(\hat{u} \cdot \hat{R}\right)^{n_{\text{sat}}} \left(\hat{u} \cdot \hat{N}\right) \left(\hat{L} \cdot \hat{N}\right) . \tag{5}$$

The latter two dot products provide the reflection cosines; the reflected flux is zero when either is negative because the surface is facing away from the observer or illumination source, respectively.

For reflected solar flux from a diffuse sphere, we apply Eq. 1, with $\cos\Phi = \left(\hat{u} \cdot \hat{L}\right)$ so that

$$F_{\text{solar}} \propto \frac{2}{3\pi r^2} \left(\sin\Phi + (\pi - \Phi)\cos\Phi\right) . \tag{6}$$

If there are multiple reflecting surfaces on the satellite, we treat each separately and additively combine their respective fluxes; shadowing effects are not modeled. We illustrate the geometry in Fig. 1.

Depending on the relative positions of the satellite, Earth, and Sun, there are certain geometries for which the Earth may partially or fully eclipse the sun. In that case, we linearly scale the total reflected flux by the fraction of the solar disk that is visible at the position of the satellite. The fraction is computed by an overlapping-circles calculation [16].

3.7 Earthshine Models

3.7.1 Simple Diffuse-Sphere Earthshine (Cognion)

Now we arrive at our first earthshine model. We consider the planet as a simple diffuse sphere, which was shown to be an effective approximation for satellites in GEO, as described in Sec. 2. We evaluate earthshine reflection from the following elements, noting that we reuse symbols from the previous section with new definitions:

1. $\hat{L}$: unit vector pointing from Earth to sun
2. $\hat{v}$: unit vector pointing from Earth to satellite
3. $\hat{u}$: unit vector pointing from satellite to observer
4. $\hat{N}$: unit normal vector of the satellite surface element (not needed for a diffuse sphere component)
5. n_{sat}: satellite shininess parameter (0 for diffuse surface)
6. d: range from satellite to sensor
7. ρ: range from center of Earth to satellite

Once again we have set $K \equiv 1$ for the satellite body. We *also* assign $K_E \equiv R_E^2$; the inclusion of the squared Earth radius allows us to fit a roughly unit scale parameter for the Earth reflectivity.

Incident sunlight reflects off Earth to the satellite according to the diffuse sphere equation, (1), with $\cos\Phi = \left(\hat{v} \cdot \hat{L}\right)$;

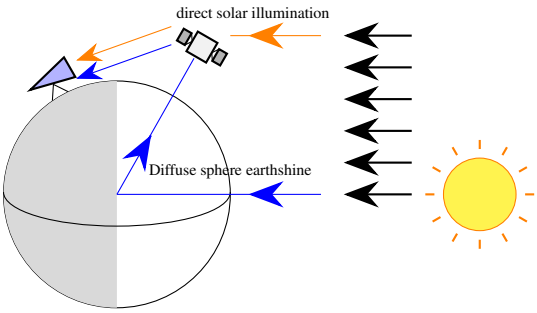

Fig. 3: In the simple diffuse-sphere model of earthshine, we treat the Earth as a distant diffuse reflecting sphere. This ball reflects light toward the satellite, which is then reflected back to the observer.

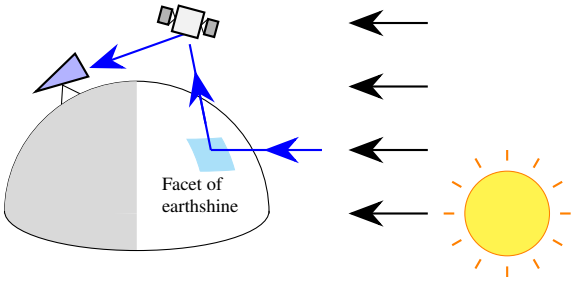

Fig. 4: In the faceted-Earth model, we discretize the surface of the planet into small plates and treat each as an independent reflector of incident sunlight. The total contribution of all facets for which the sun and satellite are above local (facet) horizon is aggregated in the reflection back to the observer.

note the change here to use $\hat{v}$ since we are evaluating the reflection of sunlight off of Earth to the satellite.[3] Then the reflected earthshine flux at the satellite is proportional to

$$\tilde{F}_E \propto \frac{2R_E^2}{3\pi\rho^2}\left(\sin\Phi + (\pi-\Phi)\cos\Phi\right). \tag{7}$$

Once we have evaluated the reflected flux to the satellite, we apply a similar process to compute the observed flux as we did for the direct sunlight reflection, except that we replace the the illumination vector direction $\hat{L}$ with a direction vector pointing from the satellite to the center of Earth, i.e. $-\hat{v}$. We illustrate the geometry in Fig. 3.

Then the doubly-reflected (Earth then satellite) flux at the observer after reflection off a flat panel on the satellite is

$$F_E \propto \tilde{F}_E \frac{n_{\text{sat}}+2}{2\pi d^2}\left(\hat{u}\cdot\hat{R}'\right)^{n_{\text{sat}}}\left(\hat{u}\cdot\hat{N}\right)\left(-\hat{v}\cdot\hat{N}\right), \tag{8}$$

where $\hat{R}'$ is the specular direction for the incident earthshine, and again the entire expression is 0 when either of the latter two dot products is negative (including the negative sign in the second expression). Diffuse sphere satellite reflection follows analogously.

3.7.2 Faceted Sphere Earthshine

We next consider a more nuanced representation of the Earth as a discretized "disco-ball" sphere made up of a collection of flat plates, or facets. The total earthshine flux is evaluated by summing over the contributions of all facets. Compared to a monolithic diffuse sphere model, the faceted approach enables more fine-grained processing of the local facet orientation and geometry, relative to the satellite and sensor. There are myriad methods for robustly discretizing a sphere; one approach was presented in [7], and we mention two alternative libraries below.

To calculate the reflected earthshine flux, we treat each facet as a flat reflecting plate with a normal vector oriented in the radial outward direction. We normalize the effective reflectivity of facet i to the surface area of the facet, $K_i \equiv A_i$. Altogether we need the following parameters for each facet, where i represents an index over all facets; note that the facets are positioned on the surface of a spherical Earth, so the direction vectors are referenced to the center of the facets, rather than the center of the Earth as was the case in the diffuse sphere model:

1. $\hat{L}$: unit vector pointing from Earth to sun (due to large distance to Sun, this is uniform over all facets)
2. $\hat{v}_i$: unit vector pointing from facet center to satellite
3. $\hat{u}$: unit vector pointing from satellite to observer
4. $\hat{N}_{\text{sat}}$: unit normal vector of the satellite surface element (not needed for a diffuse sphere)

[3] This differs slightly from the formulation in [6], which uses the vector from *sensor* to satellite, whereas we use the vector from *Earth* to satellite. The vectors may differ by an angle as large as $\arcsin(R_E/\rho)$; thus for RSOs near GEO, these vectors are nearly parallel due to the large distance so the distinction is minor, while in LEO the vectors may be substantially different. The choice of Earth-centered sun angle aligns better with the model's approximation that earthshine originates from a point at Earth's center.

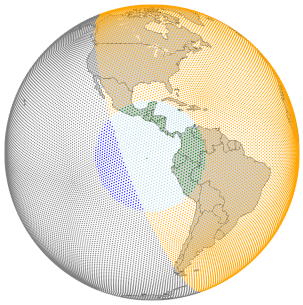

Fig. 5: Example decomposition of Earth's surface into 41150 hexagonal + 12 pentagonal facets using the `h3` library, corresponding to four levels of cell subdivisions. Facet centers have been colored according to whether they are illuminated by the sun (at $+20^\circ$ elevation) and/or visible to a 500km satellite crossing the equator. The visible region has been segmented into water (blue) and land (green) by the `global-land-mask` library.

5. $\hat{N}_i$: unit normal vector of the facet (Earth radial direction)
6. n_{sat}: satellite shininess parameter (0 for diffuse surface)
7. n_i: facet shininess parameter (0 for diffuse surface)
8. d: range from satellite to sensor
9. ρ_i: range from facet center to satellite

Then the earthshine flux at the satellite from facet i is

$$\tilde{F}_E^{(i)} \propto A_i \frac{n_i+2}{2\pi\rho_i^2} \left(\hat{v}_i \cdot \hat{R}_i\right)^{n_i} \left(\hat{v}_i \cdot \hat{N}_i\right) \left(\hat{L} \cdot \hat{N}_i\right), \tag{9}$$

where $\hat{R}_i$ is the specular direction for that facet. The flux is zero when either of the latter two cosines are negative, which occur when either the satellite cannot see that facet or the facet is not illuminated by the sun, respectively. Then we compute the reflection of the facet flux off the satellite component(s) to the observer, as illustrated in Fig. 4. The total flux at the observer is obtained by the sum over all facets, e.g. for a flat satellite surface, we obtain

$$F_E \propto \sum_i \tilde{F}_E^{(i)} \frac{n_{\text{sat}}+2}{2\pi d^2} \left(\hat{u} \cdot \hat{R}_i'\right)^{n_{\text{sat}}} \left(\hat{u} \cdot \hat{N}_{\text{sat}}\right) \left(-\hat{v}_i \cdot \hat{N}_{\text{sat}}\right), \tag{10}$$

where the specular direction $\hat{R}_i'$ is computed from the satellite surface normal $\hat{N}$ and facet direction vector $-\hat{v}_i$. It is important to recognize that there are multiple independent parameters to be fit by the data-driven method: the individual facet reflectivities in (9), and an overall satellite surface reflectivity in (10).

We considered several numerical methods for decomposing the Earth into facets, including bespoke custom implementations as well as mature libraries such as `trimesh` [17] that creates a triangular mesh and `h3` [18] that splits the sphere into hexagonal and pentagonal cells. Ultimately we found the `h3` library well suited for faceted earthshine modeling due to its specific design choices for geospatial applications. The Earth is partitioned into a hierarchical grid of hexagonal cells (plus 12 pentagons), starting from an initial tesselation with 122 hexagons and recursively subdividing. As with the `trimesh` library, `h3` provides numerous relevant utilities to efficiently compute key geometric quantities. Moreover, the native geocentric coordinate system ensures consistent surface alignment of facets over time and couples conveniently with the `global-land-mask` library which allows rapid segmentation into land and water regions as illustrated in Fig. 5. The faceted model could be extended to albedo maps of the planet in the future as well.

3.7.3 Integrated Earthshine

In the infinitely-faceted limit, our disco-ball summation becomes an integral over infinitesimal surface elements. We introduce a new integral formulation leveraging a specific coordinate frame definition hereby defined as the *integral frame*. In this frame, $\vec{V}$ represents a vector pointing from the center of the Earth to the instantaneous satellite position, $\vec{L}$ is the vector pointing from the center of the Earth to the Sun, and $\vec{U}$ is the vector pointing from the center of the Earth to the observer. We define the right-handed *integral frame* exclusively in terms of the satellite and Sun vectors such that the x-coordinate aligns with $\vec{V}$, the y-coordinate aligns with the orthogonal component of $\vec{L}$ with respect to $\vec{V}$, and the z-coordinate is orthogonal to both. Thus, the basis vectors of the integral frame obey

$$\hat{x} \propto \vec{V} \qquad \hat{y} \propto \vec{L} - \left(\vec{V} \cdot \vec{L}\right) \vec{V} \qquad \hat{z} \propto \vec{V} \times \vec{L}, \tag{11}$$

where the proportionality constants are chosen to ensure orthonormality. An illustration of this frame can be seen in Fig. 6. In the event that $\vec{V} \parallel \vec{L}$ (i.e. the Earth, satellite, and Sun positions are collinear), we are free to choose any

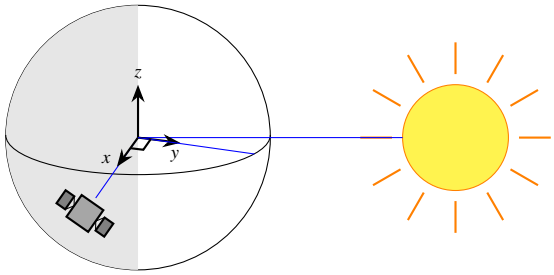

Fig. 6: An illustration of the integral coordinate frame

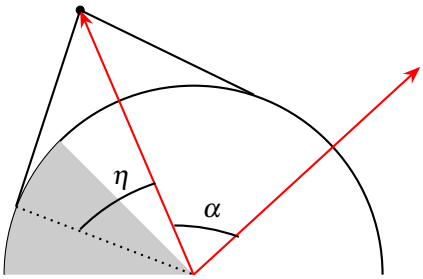

Fig. 7: An illustration of the the Satellite Earth Sun phase angle α and angle off nadir to Earth limb η.

orthogonal direction for the y-coordinate or z-coordinate – for instance, we might choose to align one with the Earth's polar axis since the Sun will never be directly over Earth's poles. Since the origin is Earth-centered, coordinates in typical Earth-centered astrodynamics representations may be rotated into this frame by a standard rotation matrix

$$M = [\hat{x}\ \ \hat{y}\ \ \hat{z}]^\top . \tag{12}$$

We turn next to the integral formulation. We define a spherical representation over our integral frame, where $\theta \in [0, \pi]$ is the angle from the $+z$ polar axis and $\phi \in [-\pi, \pi]$ is the azimuthal angle from the x-axis (aka the satellite direction vector). For an infinitesimal surface element at position (R_E, θ, ϕ), the relevant earthshine parameters match those of Sec. 3.7.2 with the facet index i replaced by angular coordinates (θ, ϕ).

The earthshine flux received at the sensor results from solar flux reflecting off Earth and then reflecting off a satellite body element, so once again we need to evaluate the flux at the satellite first. The surface element has differential area $dA = R_E^2 \sin(\theta) d\theta d\phi$, hence the differential flux at satellite from this element is

$$d\tilde{F}_E(\theta,\phi) \propto \frac{n(\theta,\phi)+2}{2\pi\rho(\theta,\phi)^2} \left(\hat{v}(\theta,\phi)\cdot\hat{R}(\theta,\phi)\right)^{n(\theta,\phi)} \left(\hat{v}(\theta,\phi)\cdot\hat{N}(\theta,\phi)\right) \left(\hat{L}\cdot\hat{N}(\theta,\phi)\right) R_E^2 \sin(\theta) d\theta d\phi\,. \tag{13}$$

The proportionality constant may also vary over the integral region, e.g. due to varying surface albedo. We address this by partitioning the Earth into land and water regions and fitting independent coefficients for each region.

We multiply (13) by the BRDF and direction cosines at the satellite, yielding the differential observed flux:

$$dF_E \propto d\tilde{F}_E(\theta,\phi) \frac{n_{\text{sat}}+2}{2\pi d^2} \left(\hat{u}\cdot\hat{R}'(\theta,\phi)\right)^{n_{\text{sat}}} \left(\hat{u}\cdot\hat{N}_{\text{sat}}\right) \left(-\hat{v}(\theta,\phi)\cdot\hat{N}_{\text{sat}}\right) . \tag{14}$$

Finally, we integrate over all surface elements that are both in view of the satellite and illuminated by the sun. The chosen coordinate frame allows us to express those integral bounds cleanly in terms of the satellite's local horizon and the Earth-centered solar angle α between the satellite and sun vectors. The satellite's local horizon occurs at an Earth-centered angle from the x-axis defined by

$$\cos\eta = \frac{R_E}{R_{\text{sat}}}\,, \tag{15}$$

where $R_{\text{sat}} = R_E + \text{altitude}$ is the satellite's distance from the center of the earth. The flux from any portion of Earth outside of the η circle will not contribute to the observed brightness. The solar angle is defined by

$$\cos\alpha = \frac{\vec{V}\cdot\vec{L}}{||\vec{V}||\,||\vec{L}||}\,. \tag{16}$$

Because we aligned the x-axis with $\vec{V}$, this is the first coordinate of the transformed illumination vector $M\vec{L}$. The choice of coordinate system ensures the terminator traces a great circle at a fixed azimuthal coordinate $\phi_0 = \alpha - \pi/2$ on the hemisphere with positive x-coordinate. We illustrate the geometry of both angles in Fig. 7.

Now we have everything needed to express the integral bounds. There are two cases to consider. When the terminator falls outside of the local horizon, we integrate over the entire visible portion of the surface. Otherwise, we clip the

lower bound of the ϕ integral at ϕ_0. This makes intuitive sense. When the Sun is nearly above the satellite in the sky, the entire visible surface will be illuminated. However, when the satellite is near the terminator, only a portion of its visible Earth will be illuminated. We express the bounds on θ as a function of ϕ such that the integral only spans the portion of Earth within the visible horizon. Then the complete set of integration bounds are:

$$\max(-\eta, \phi_0) \leq \phi \leq \eta \tag{17}$$

$$\frac{\pi}{2} - \arccos\left(\frac{R_E}{R_{\text{sat}}|\cos(\phi)|}\right) \leq \theta \leq \frac{\pi}{2} + \arccos\left(\frac{R_E}{R_{\text{sat}}|\cos(\phi)|}\right). \tag{18}$$

Although the expression in (14) looks rather complicated on paper, Slingshot has developed an object-oriented method to implement and evaluate this model with numerical integration techniques. In Appendix A, we analytically evaluate the integral in the limit of large altitude and show that this integral formulation recovers the diffuse sphere expression in that limit, which explains why the diffuse sphere earthshine model works well for GEO RSOs.

3.8 Model Fits

In the methodology adopted for this analysis, we leverage fitting methods that enable discovery of data-informed approximations for the unknown model parameters and evaluate the relative quality of those estimates on both seen and unseen data. There are a number of proportionality constants that may be determined by fits to data. We obtain these parameters by generating observed flux predictions with the model(s), converting those to apparent magnitudes, and jointly optimizing the coefficients to minimize the mean square error (MSE) between the model predictions and real observed magnitudes. Specifically, we allow one free effective reflectivity parameter per satellite surface reflection type, and one free effective reflectivity parameter per earthshine source (e.g. diffuse land, diffuse water, specular water, etc). The solar illumination source is configured with a static coefficient of 1 since it is always present, and any misconfiguration of scale in this parameter, relative to the observational data scale, will be absorbed as an overall scale factor in the reflectivity coefficients. For that reason, we advise against direct physical interpretation of the fitted parameters. We write this compactly in terms of the fitted illumination source coefficients C_i and surface coefficients D_j

$$F_{\text{predicted}} = \sum_i C_i \sum_j D_j F_{ij}\,, \tag{19}$$

where i indexes over illumination sources, and j indexes over satellite surfaces; $C_0 \equiv 1$ represents the direct solar illumination source. The fluxes F_{ij} are computed individually for each illumination source (i) and satellite surface type (j). Furthermore, in the event that the input data contains more than one class of satellite buses, we fit a separate set of D_j coefficients for each class, while sharing the illumination coefficients C_i over all classes. We convert the predicted flux $F_{\text{predicted}}$ to magnitude $m_{\text{predicted}}$ with (2) and minimize the MSE loss function over $\mathcal{N}$ observed data points:

$$J = \frac{1}{\mathcal{N}} \sum_{k=1}^{\mathcal{N}} \left(m_{\text{predicted},k} - m_{\text{observed},k}\right)^2. \tag{20}$$

Table 2 expresses the model combinations we consider, along with the various satellite configurations. Results will be reported for the cartesian product over all elements listed in the tables. We evaluate quality of the fitted models over the observational data according to two values: Residual MSE – **Lower is better** – and Pearson correlation coefficient (PCC), also known as the R-value – **Higher is better**.

We further assess the predictive power of the fitted models using unseen data from dates outside the range of the fitted data. Those dates will generally have different aggregate illumination conditions than the training period due to seasonality and orbital mechanics. This provides a quantitative assessment of the models' practical utility for estimating future observability in the presence of earthshine. We also perform a small ablation study over the length of time covered by the input data, evaluating performance over the same unseen observations.

4. RESULTS

4.1 Simulated Data

4.1.1 Flux at Satellite Earthshine Model Comparison

Turning now to the model results and comparisons, we begin with an investigation using synthetically generated data before moving onto the fitted analyses. For initial comparison, we compute and visualize the predicted earthshine

Table 2: Illumination source and surface geometry details for the models considered in this analysis, where each row represents one model configuration. A *D* in the box indicates that we include that column's illumination source or surface type as a diffuse reflector, an *S* in the box indicates we include it as a specular reflector (with independent coefficient from the diffuse component), and *X* indicates that solar illumination is included.

Illumination source	Solar	Land	Water
Sunshine only	X		
Sunshine + diffuse Earth	X	D	D
Sunshine + Phong Earth	X	DS	DS

Sat surface geometry	Sphere	Nadir Face	Solar Panel (sun)	Solar Panel (back)
Diffuse sphere	D			
Phong sphere + panels	DS		DS	DS
Phong box + panels		DS	DS	DS
Phong all	DS	DS	DS	DS

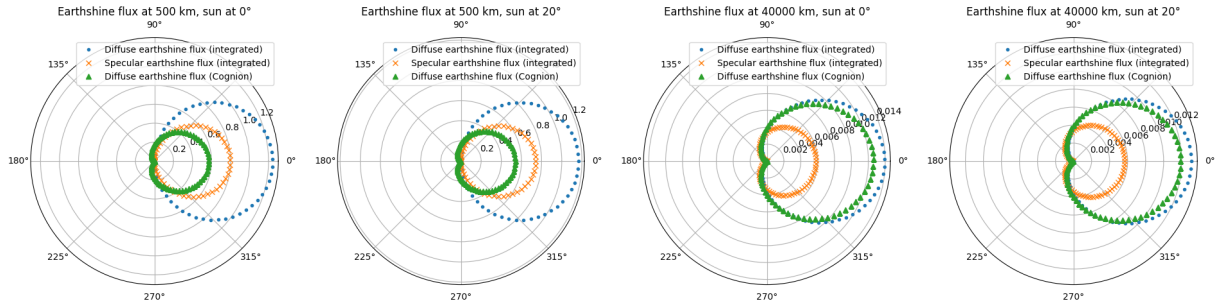

Fig. 8: Earthshine flux at 500km and 40000km altitudes for an equatorial satellite and two sun positions. The pure diffuse-sphere model of earthshine (7) agrees well with the integrated approach (integral of (13)) for RSOs near GEO, but departs substantially for LEO RSOs.

flux at the satellite position by the diffuse-sphere and integrated earthshine models, with arbitrary normalizations of reflectivity parameters. In this portion, we do not model a sensor location since we are only interested in the flux at the satellite. The sun is fixed at 0° on the polar plots in Fig. 8, looking down from above the Earth's north pole.

In each case, earthshine is strongest on the day-side of Earth, and there is a rapid drop off in flux reaching the satellite from regions near the terminator. For the equatorial LEO satellite, there is virtually no earthshine contributing to observed brightness on the far night-side of the Earth, as one might expect. However, Fig. 8 reveals a striking qualitative difference between the diffuse-sphere model of earthshine and the integrated model for LEO satellites: the diffuse-sphere model flux persists substantially further past the terminator because the diffuse-sphere model does not account for the limited portion of surface visible to the satellite, while the integrated model incorporates more realistic geometric constraints. Meanwhile, for RSOs at much higher altitudes, both models of diffuse earthshine produce quite similar results because most of the Earth disk is visible to those satellites, so the full diffuse-sphere approximation is more appropriate; see also Appendix A.

Next we generate similar plots for the 500km, 0° case in Fig. 9 to compare the faceted earthshine model with the integrated model and investigate the tradeoffs in model quality with varying facet counts. We observe poor model quality across both specular and diffuse earthshine at low facet numbers, with specular reflections requiring higher facet counts to converge on the integrated earthshine patterns. The legend highlights that the mean absolute percentage error (MAPE) relative to the integrated model decreases with rising facet counts, dropping below 10% between 842 and 5882 facets and below 1% between 5882 and 41162 facets; the 99$^{\text{th}}$ percentile relative percentage error (p99 err) follows suit though remaining close to 1% even at the highest tested resolution.

4.1.2 Flux at Sensor Earthshine Model Comparison

The satellite brightness observed at a sensor must account for reflection off of the various satellite surfaces. To that end, we apply both the integrated earthshine model and direct solar illumination to each of the representative surface types and predict the flux at a fixed equatorial sensor location; multiple locations were considered, and we report one illustrative case here. The portion of sky viewable to the sensor is marked, and the effective reflectivity of each object is unit normalized. Fig. 10 shows predicted sensor fluxes with the sensor placed at $\varphi = 67.5°$ (in daylight). Although

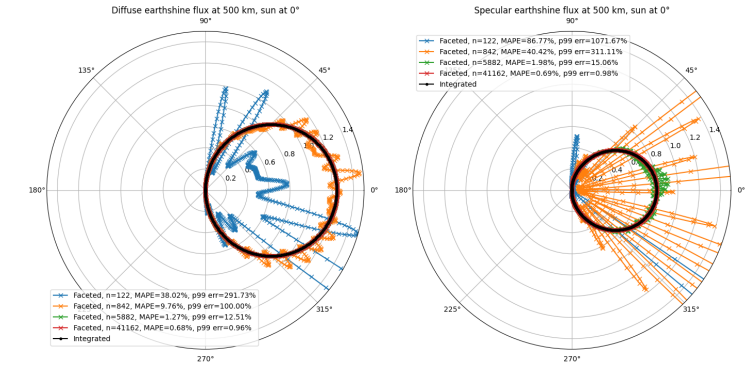

Fig. 9: Earthshine flux at 500km for an equatorial satellite and the sun at 0° elevation. The faceted model (9) is highly irregular at low facet counts, and converges on the integrated model (integral of (13)) at higher facet counts.

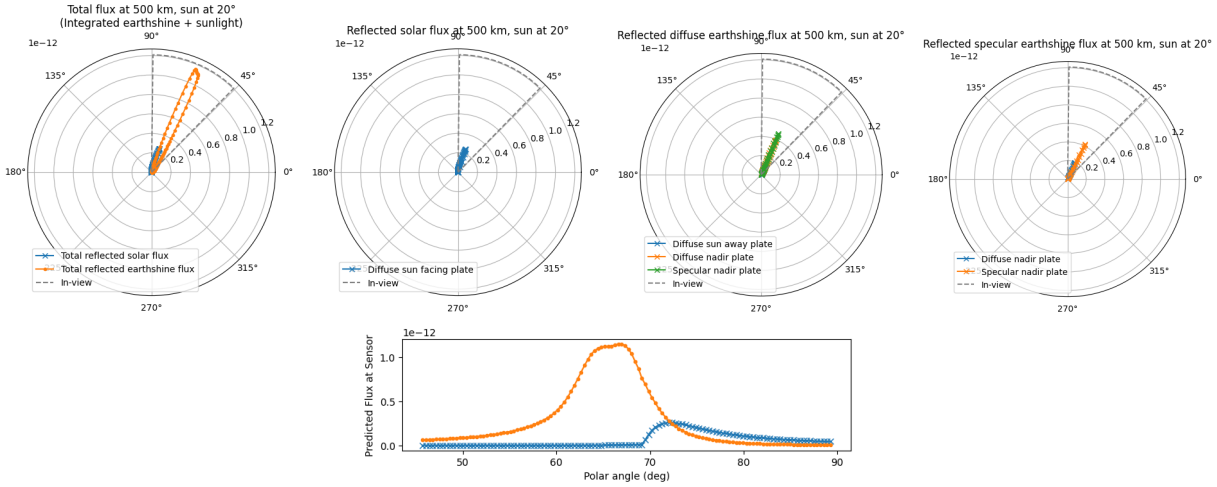

Fig. 10: Top: Reflected flux due to direct solar reflection and earthshine for an equatorial satellite; the sun is set at an elevation of 20°. The left plot shows total contributions, and the other plots break out into components. Bottom: Close-up visible portion of the left-most polar plot as a function of φ, highlighting the relative dominance of earthshine.

all types of reflecting surfaces were modeled, only those contributing $> 10^{-13}$ to the flux are shown for clarity. For this geometry, earthshine is seen to be the dominant illumination source over a range of angles.

We also observe that the faceted earthshine approach suffers additional degradation compared to the integrated model when accounting for satellite surface reflections, compared to the prior analysis that only considered flux at the satellite. Fig. 11 shows that both MAPE and p99 err remain large even with over 40,000 facets.

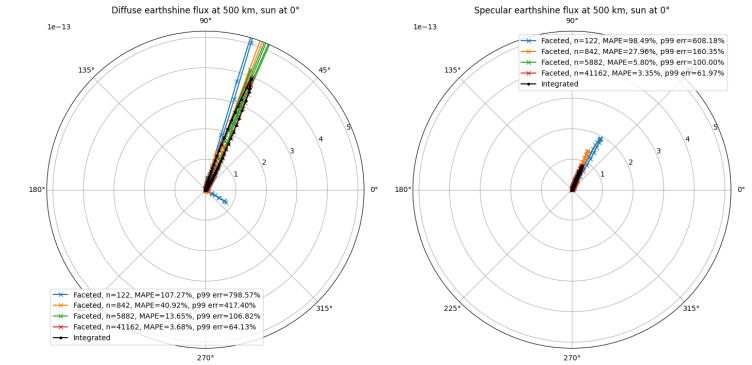

Fig. 11: Comparison of faceted Earth calculations to the integral method, accounting for reflections off all modeled satellite body surfaces, with relative error statistics reported in the legend.

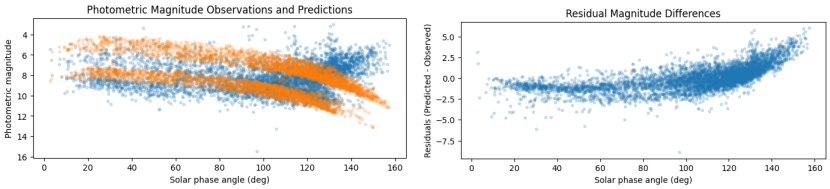

Fig. 12: Left: Observed (blue) and predicted (orange) magnitude versus solar phase angle from the best fit model using only direct solar illumination and a simple diffuse sphere model for each satellite. The banding occurs principally due to the range differences among observations of the various bus families with Starlink and Iridium generally falling in the upper, brighter band, and Arrow and Globalstar in the dimmer band. Right: Fit residuals. There is clear structure in the residuals, especially at large phase angles.

4.2 Real Data

Finally, we present results of fitting the unknown parameters in our models with real world observations. All fits were performed jointly over the full set of satellite bus classes, and we only report results generated from direct solar illumination and the integrated earthshine model, due to the findings from the previous sections that the integrated model better accounts for local geometry than the diffuse-sphere model for LEO RSOs. We found the integral approach easier to scale than the faceted method due to memory requirements and speed benefits in certain cases, and it does not suffer from subdivision sensitivity. Hence we report real-data results generated from the integral approach.

To estimate Earth and satellite shininess, we scanned over a grid of shininess parameters, spanning 10, 100, and 200 for each; each experiment was run against the full set of model configurations. Our final results use 10 and 100, respectively, selected after heuristic fit-quality comparisons on a subset of results. When the multiplicative effects of the experiments and parameter grid search are taken into account, the dataset required 265 million transformations, including positioning, relative coordinate translations, faceted surface calculations, and integrals. The grid of nine experiments was completed in under 24 hours using distributed storage and multiprocessing.

We present four case studies on a selected set of models by which we identify the critical portions where our analysis indicates that earthshine is a significant contributor to the total observed illumination. We then tabulate the complete fit results and evaluations in two sections: first the evaluation metrics for fits generated from a dataset spanning 01 Jan - 08 Jan 2025 and evaluated on unseen observations from 17 Jan - 31 Jan 2025, followed by evaluation metrics for fits generated from a longer input time series spanning 01 Jan - 16 Jan 2025 and evaluated on the same unseen dates.

4.2.1 Case Study: Sunshine Only, Diffuse Sphere Satellite

For our first case study, we consider only direct solar illumination and a satellite representation consisting of only a single diffuse sphere body element. This simple model works reasonably well for many observations at intermediate phase angles. However, it is readily apparent in Figs. 12 and 17 (left) that this model breaks down for certain illumination conditions, most notably at large phase angles where the solar reflectance off a diffuse sphere declines rapidly while the true observations trend slightly upwards. The curving residuals in the right hand plot make this quite clear, and the correlation between predictions and observations is only $R = 0.50$. There is a clear trend difference, especially at large phase angles, as well as some notable peaks that are not captured by this model.

4.2.2 Case Study: Sunshine + Phong Earthshine, Diffuse Sphere Satellite

Next we consider the same simple satellite geometry with the addition of four earthshine illumination sources: diffuse and specular land, and diffuse and specular water. Indeed Fig. 13 illustrates that the addition of earthshine enables the fit to better approximate certain aspects of the large phase angle magnitudes, and the residual plot shows a substantially reduced upward trend at large Φ. The correlation coefficient between predictions and observations improves to $R = 0.55$. However, some structure remains in the residuals, including a strong bump around $130^\circ - 140^\circ$.

4.2.3 Case Study: Sunshine Only, Phong Box + Phong Panels

It was observed in [7] that specular reflections off the nadir face of a Starlink satellite are important contributors to the observed brightness, especially around $130^\circ - 140^\circ$ solar phase angles. However, their data set became quite sparse at higher phase angles, so here we investigate whether a reflective nadir face with solar panels provides sufficient reflected sunlight to capture the previously noted residuals without needing to incorporate earthshine at all.

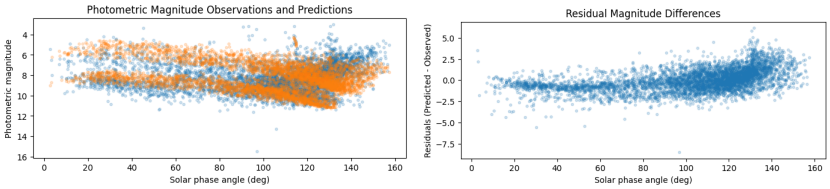

Fig. 13: Left: Observed (blue) and predicted (orange) magnitude versus solar phase angle from the best fit model using direct solar illumination plus Phong earthshine and a diffuse sphere model for each satellite. Right: Fit residuals. The overall trend at large phase angles has been substantially reduced, though some structure remains in the residuals.

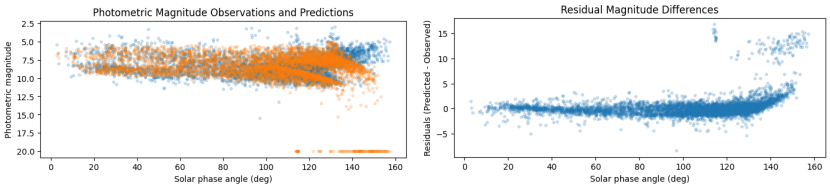

Fig. 14: Left: Observed (blue) and predicted (orange) magnitude versus solar phase angle from the best fit model using only direct solar illumination and a nadir-facing box plus solar panels model for each satellite. Right: Fit residuals. The bump in residuals at mid-large phase angles has been partially reduced, but at the cost of a huge increase in residuals for nighttime observations at very large phase angles and daytime observations at intermediate phase angles.

We confirm in Fig. 14 that in the absence of earthshine, the presence of a nadir-facing panel does seem to address a portion of the observed residuals; most notably it is a possible source for the bump around 130°. However, the shape of the specular lobe is not sufficient to explain the broader rise in observed magnitude at higher phase angles. In fact, it is necessary to clip the predicted fluxes and adjust the fit's loss function for certain observations to avoid NaNs because the box + panels geometry with only solar illumination is unable to produce sufficiently large fluxes to avoid numerical issues in the conversion to magnitudes. The clipping is also responsible for the blobby artifacts that appear in the residuals plot. The correlation coefficient is near zero for the fit due to those observations as well.

In our view, this provides clear evidence of the need to accurately account for earthshine in LEO brightness estimates.

4.2.4 Case Study: Sunshine + Phong Earth, Phong Box + Phong Panels

Bringing together the previous findings by including both earthshine and a nadir-box plus panels satellite representation, we see marked improvement in the fit across nearly all solar phase angles. There are a small collection of narrow-banded artifacts visible in Fig. 16 for which large residuals appear due to mismodeled specular reflections; however the overall trends and structures are generally well described by this system. The righthand scatter plot in Fig. 17 shows much tighter correlation compared to the diffuse sphere sunshine plot on the left, with $R = 0.79$ versus 0.50. We note that daytime observations constitute only a small fraction of the observations, yet it is evident from Figs. 16 and 17 that even those bright daytime objects, for which we have seen that earthshine can be a critical component, are reasonably well fit by this model.

We also highlight the predicted contributions of different components to the observed magnitudes of Starlink v1.5 satellites in the full, unsampled Horus dataset in Fig. 15. The figure can be compared with Fig. 7 in [7], where we have marked the region where earthshine becomes significant. We note the specular reflections of sunlight off the solar panels (red in the middle plot), create a low phase-angle artifact that is not present in the observations; this may be due to our pointing approximations that do not fully account for real world Starlink v1.5 panel dynamics.

4.2.5 Fit Evaluation Metrics

Table 3 contains the evaluation metrics for fits generated using observations from the first week of January 2025, and Table 4 reports similar metrics for fits generated with two weeks of data. Both versions used the last two weeks of the month for unseen data evaluations. It is apparent from these results that a) earthshine is an important factor in modeling LEO RSO brightness as the MSE is lower and correlation coefficient higher across all satellite geometry representations when earthshine is included; b) even when earthshine is included, it is important to account for nadir-facing satellite surfaces on the satellite bus, as a simple sphere with or without solar panels does not capture the relevant

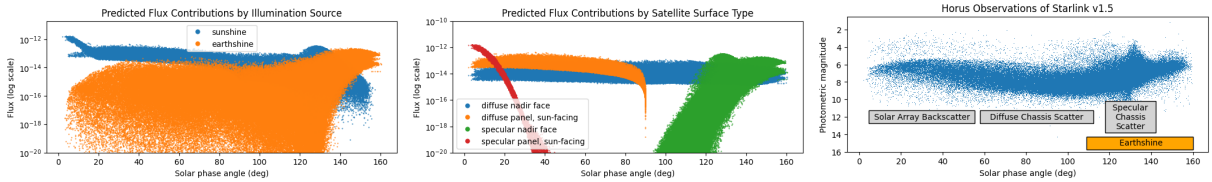

Fig. 15: Left, middle: Predicted flux contributions of various illumination sources and reflective surfaces to Horus observations of Starlink v1.5 satellites. Right: Annotated observations; compare annotations to Fig. 7 in [7].

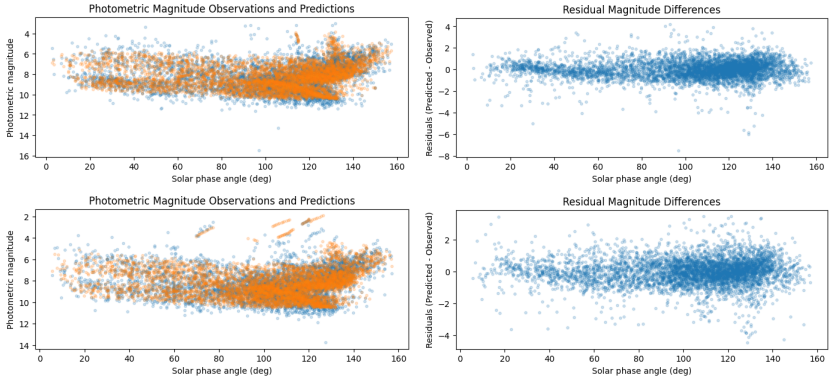

Fig. 16: Top: Data from fit period. Bottom: Unseen data. Left: Observed (blue) and predicted (orange) magnitude versus solar phase angle from the best fit model using direct solar illumination plus diffuse and specular earthshine and a nadir-facing box plus solar panels model for each satellite. Right: Fit residuals. The residual plot is centered and uniform across the full range of phase angles, indicating that the satellite geometry and earthshine modeling provide an adequate representation of the observed magnitudes. The performance on unseen data is comparable to the fit performance, demonstrating effective extrapolation, even on bright objects not seen during the fit period.

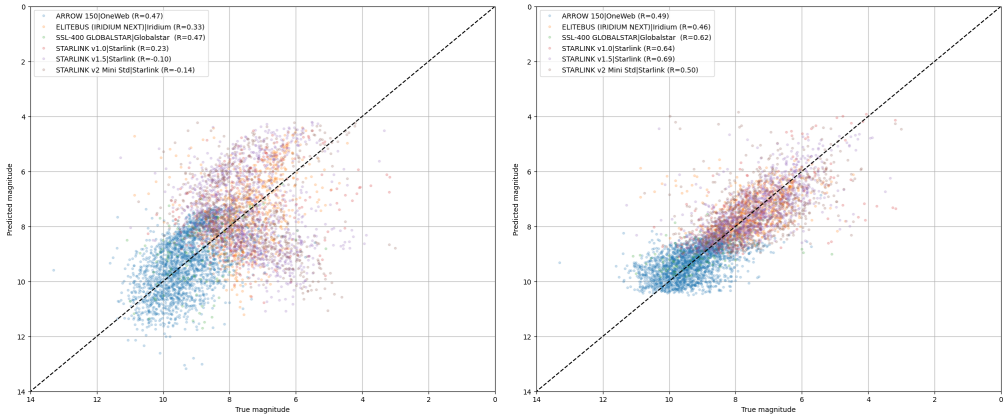

Fig. 17: Observations compared to predicted magnitude for several bus families from the best fit models using: Left – only direct solar illumination and a simple diffuse sphere model for each satellite, the PCC for this scatter plot is $R = 0.50$; Right – direct solar illumination plus diffuse and specular earthshine and a nadir-facing box plus solar panels model for each satellite, the PCC for this scatter plot is $R = 0.79$.

Table 3: Fit evaluation metrics for models using training data spanning 01 January - 08 January 2025.

Model description (Illumination, Sat Config)	MSE – Fit	PCC – Fit	MSE – Unseen	PCC – Unseen
Sunshine only, diffuse sphere	2.05	0.52	2.09	0.54
Sunshine only, Phong sphere + Phong panels	1.34	0.61	1.18	0.68
Sunshine only, Phong box + Phong panels	1790.76	-0.11	1894.80	-0.21
Sunshine only, Phong all	1.16	0.65	1.16	0.65
Sunshine + diffuse Earth, diffuse sphere	1.59	0.59	1.62	0.66
Sunshine + diffuse Earth, Phong sphere + Phong panels	1.13	0.67	1.11	0.73
Sunshine + diffuse Earth, Phong box + Phong panels	0.69	0.80	0.68	0.80
Sunshine + diffuse Earth, Phong all	0.67	0.80	**0.66**	**0.82**
Sunshine + Phong Earth, diffuse sphere	1.50	0.60	1.72	0.66
Sunshine + Phong Earth, Phong sphere + Phong panels	1.10	0.67	1.15	0.73
Sunshine + Phong Earth, Phong box + Phong panels	0.63	0.81	0.71	0.81
Sunshine + Phong Earth, Phong all	**0.61**	**0.82**	0.69	**0.82**

Table 4: Fit evaluation metrics for models using training data spanning 01 January - 16 January 2025.

Model description (Illumination, Sat Config)	MSE – Fit	PCC – Fit	MSE – Unseen	PCC – Unseen
Sunshine only, diffuse sphere	2.16	0.50	2.07	0.55
Sunshine only, Phong sphere + Phong panels	1.37	0.60	1.31	0.68
Sunshine only, Phong box + Phong panels	1913.53	-0.10	1948.06	-0.24
Sunshine only, Phong all	1.30	0.63	1.31	0.62
Sunshine + diffuse Earth, diffuse sphere	1.73	0.56	1.58	0.66
Sunshine + diffuse Earth, Phong sphere + Phong panels	1.24	0.64	1.14	0.75
Sunshine + diffuse Earth, Phong box + Phong panels	0.75	0.78	0.71	0.82
Sunshine + diffuse Earth, Phong all	0.73	0.78	0.71	0.82
Sunshine + Phong Earth, diffuse sphere	1.68	0.55	1.56	0.66
Sunshine + Phong Earth, Phong sphere + Phong panels	1.29	0.62	1.22	0.73
Sunshine + Phong Earth, Phong box + Phong panels	0.72	**0.79**	0.69	0.82
Sunshine + Phong Earth, Phong all	**0.69**	**0.79**	**0.68**	**0.83**

reflections as well; and c) slight incremental improvement was seen when both sphere and nadir-panel geometries were included, potentially because the sphere was able to approximately capture off-nadir structure, but the overall enhancement was small compared to the effect of replacing the sphere with a nadir-panel representation.

We also observe that the extension to two weeks of fit data had only slight impacts to the fit evaluation metrics of most models, although the unseen data metrics show somewhat more consistent generalization among the two-week models, especially those with more complexity. Overall this indicates that even one week of observations data tends to capture the primary contributing factors quite well and two weeks of data enables further refinement of the predictions among the considered satellite bus families and illumination geometries.

5. DISCUSSION AND FUTURE WORK

We have investigated several families of RSO brightness models in the presence of both direct solar and reflected earthshine illumination sources. Representative satellite body and panel geometries were considered for their effects on the reflection of light to a ground-based observer. Our synthetic data analysis demonstrated three key takeaways:

1. Earthshine is predicted to be an important contributor to LEO RSO brightness, especially at large solar phase angles, and can even dominate reflected solar illumination under certain geometric conditions.
2. The traditional model of earthshine as originating from a large diffuse sphere may be valid for GEO RSOs but is not applicable for LEO RSOs due to the limited portion of Earth visible from the lower altitudes.
3. A faceted-sphere model of Earth better accounts for the local scattering geometry than the simple diffuse sphere model, but a large number of facets is required to obtain results consistent with a direct integration approach.

Without making detailed assumptions about specific satellite body sizes, shapes, and reflectivity characteristics, we

applied our models to real world observations and inferred values for unknown model parameters from a best fit algorithm. The fitted models extrapolated consistently to unseen data, providing evidence that our methodology can be practically relevant for predicting future RSO brightnesses.

The data-driven approach enabled us to compare performance metrics across a variety of different models, both with and without earthshine, from which we were able to identify which model characteristics provide the best approximation to real world observations. Our results indicate the following:

1. We confirmed the expectation, based on the synthetic data analysis above, that earthshine would be an essential element to consider for LEO object brightness prediction, especially at large solar phase angles and in daytime viewing conditions when a large portion of illuminated Earth surface may reflect off the satellite.
2. We replicated the findings from [7] that diffuse sphere satellite geometry does not accurately describe reflections off Starlink chassis, and that nadir-face reflections substantially improve fit quality.
3. We showed that our data-driven analysis technique is applicable to a variety of satellite bus families, and provides concrete predictive power on unseen data.

We also note a few practical trade-offs. First, the trade between speed and compute power; the more machines available for computation, the faster the dataset can be run. The speeds achieved for this experiment are well within the bounds of useful operational cadence, especially given the data that would be gathered over the course of a single day rather than a month. Additionally, during experiments with faceted models, exponentially more time was spent was on object representations with higher numbers of facets. The accuracy of the results could be traded for faster compute times with lower-fidelity representations. Detailed experimentation could be performed on each sensor system to identify necessary compute requirements to obtain sufficient predictive accuracy.

Looking beyond the current results, we believe this methodology could unlock new value from unresolved photometric light curves, besides the traditional SDA tracking applications. For instance, although we have not explored physical interpretations of the parameters produced by our methods due to interrelations among the fits and scale factors assumptions, there may be interesting insights hidden in the outputs. Given the large number of photometric observations produced by optical fences, one may be able to infer an empirical albedo map of Earth's surface, potentially even accounting for time-dependent effects such as weather and ground cover that influence the surface reflectivity.

The fitted RSO reflectivity parameters may also encode information about the size and materials that make up the satellite components. An investigation into the relationship among those quantities for known bus models could be a fruitful subject for follow-up work, potentially enabling one to reconstruct an effective optical cross section from unresolved imagery. This has connections to prior and ongoing work related to RSO fingerprinting, anomaly detection, and light curve analyses. For instance, changes in the inferred optical cross section could indicate an attitude shift or physical reconfiguration with important implications for tracking and safety monitoring.

It is also notable in Fig. 17 that, while Starlink fits improved substantially from the inclusion of earthshine and additional bus geometries, this was not true to the same degree for all bus families. It would be interesting to better understand the bus geometries and operational patterns of those constellations to see which assumptions may be less applicable to those RSOs. It would also be interesting to expand this analysis to other families of objects, especially tumbling and debris where higher-frequency temporal variations cannot be neglected.

More generally, we emphasize the importance of including sufficiently high-fidelity earthshine effects in simulations, predictions, and analyses of LEO RSO light curves. Optical data provide critical inputs to LEO SDA, and accurate brightness models are a key input to efficiently utilizing those resources. We look forward to the continuing development of related technologies that further unlock the latent information within photometric observations.

6. REFERENCES

[1] ESA Space Debris Office. Esa's annual space environment report, 2025.

[2] E.M. III Vallerie. Investigation of Photometric Data Received from an Artificial Earth Satellite. Master's thesis, Air Force Institute of Technology, Wright-Patterson AFB, OH, Aug 1963.

[3] Rita L. Cognion. Large phase angle observations of GEO satellites. In Khanh D. Pham, Joseph L. Cox, Richard T. Howard, and Genshe Chen, editors, *Sensors and Systems for Space Applications VI*, volume 8739, page 87390K. International Society for Optics and Photonics, SPIE, 2013.

[4] Ho Jin, Yongjun Song, Yongseok Lee, and Kap-Sung Kim. The light curves of a geostationary satellite and its model. *AMOS Proceedings*, 2011.
[5] P North, P Zimmer, T.S. Kelso, Daniel Oltrogge, Thomas Johnson, R Hall, and J Cooper. Ssa degradation from large constellations: A starlink-based case study. In *International Conference on Space Situational Awareness Arlington, VA, USA IAA-ICSSA-20-00-20*, 01 2020.
[6] Rita L Cognion. Observations and modeling of GEO satellites at large phase angles. *AMOS proceedings*, 2013.
[7] Forrest Fankhauser, J Anthony Tyson, and Jacob Askari. Satellite optical brightness. *The Astronomical Journal*, 166(2):59, 2023.
[8] Sarah Caddy and Lee Spitler. A Surprising Boost in Starlink Satellite Brightness at OpticalWavelengths During the Day. *AMOS Proceedings*, 2024.
[9] Dr Jovan Skuljan. untitled, 09 2019. Explanation of corrections distance from earth center and cosine fall off of earthshine contribution to solar array panels.
[10] Sarah E. Caddy and Lee R. Spitler. Daytime Photometry of Starlink Satellites with the Huntsman Telescope Pathfinder. *The Journal of the Astronautical Sciences*, 72, Jun 2025.
[11] T Olson, C Reid, C Key, B Williams, D Witman, J Shaddix, D Kesler, and B Marchand. ML-Based Photometric Fingerprinting at Scale for LEO Satellite Monitoring. In *Advanced Maui Optical and Space Surveillance (AMOS) Technologies Conference*, page 123, 2024.
[12] Slingshot Aerospace. Linkedin post. `https://www.linkedin.com/posts/slingshot-aerospace_as-we-head-into-the-new-year-we-are-thrilled-activity-7278166438631129088-Mq2u/` [Accessed 26-08-2025].
[13] Bui Tuong Phong. Illumination for computer generated pictures. In *Seminal graphics: pioneering efforts that shaped the field*, pages 95–101. 1998.
[14] James F Blinn. Models of light reflection for computer synthesized pictures. In *Proceedings of the 4th annual conference on Computer graphics and interactive techniques*, pages 192–198, 1977.
[15] Phanindra Kandula, J Anthony Tyson, Jacob Askari, and Forrest Fankhauser. Simulated impact on LSST data of Starlink V1. 5 and V2 satellites. *arXiv preprint arXiv:2506.19092*, 2025.
[16] Eric W. Weisstein. Lens. From *MathWorld* – A Wolfram Resource. `https://mathworld.wolfram.com/Lens.html`.
[17] Dawson-Haggerty et al. trimesh. `https://trimesh.org/`.
[18] Uber Technologies, Inc. H3: Uber's Hexagonal Hierarchical Spatial Index, 2018. `https://h3geo.org/`.

A. LARGE ALTITUDE LIMIT

Here we evaluate the earthshine flux integral in the large altitude limit where $R_{\text{sat}} >> R_E$. In particular, we show that the expression for diffuse earthshine flux ($n = 0$) recovers the well-known diffuse-sphere equation (1). To derive this result, we focus on the flux at the satellite, rather than the reflected flux at the sensor, so we evaluate the integral of (13), $\int\int d\tilde{F}_E$. We leave the extension to reflected flux (14) as an exercise for the reader.

Our inputs include $\hat{L}$, a unit vector pointing toward the Sun, and $\vec{V}$, the Earth-centered position vector of the satellite. The observer position does not affect the flux-at-satellite calculation. We represent the vectors using the coordinate frame described in (11) with solar angle α as defined in (16).

Let us first address the integral limits (17) and (18). In the large altitude limit the ratio on the right hand side of (15) approaches zero, so $\eta \to \frac{\pi}{2}$, which means the distant satellite can see the entire positive-x hemisphere of the Earth. Then the ϕ bounds (17) become

$$\alpha - \frac{\pi}{2} \leq \phi \leq \frac{\pi}{2}. \tag{21}$$

Likewise, since $R_{\text{sat}}|\cos\phi| >> R_E$ everywhere except $\phi \approx \pm\frac{\pi}{2}$ (i.e., the satellite can see the entire hemisphere), the θ bounds (18) also simplify

$$0 \leq \theta \leq \pi. \tag{22}$$

Next we turn to the integrand. In the integral frame coordinate representation, the input vectors may be written

$$\vec{V} := R_{\text{sat}}\hat{V} = R_{\text{sat}}\ [1\ \ 0\ \ 0]^\top \quad \text{and} \quad \hat{L} = [\cos\alpha\ \ \sin\alpha\ \ 0]^\top. \tag{23}$$

A infinitesimal surface element has position vector

$$\vec{N}(\theta,\phi) := R_E\,\hat{N}(\theta,\phi) = R_E\,[\cos\phi\sin\theta \quad \sin\phi\sin\theta \quad \cos\theta]^\top\,. \tag{24}$$

We compute the vector $\vec{v}$ from facet to satellite as

$$\vec{v}(\theta,\phi) := \rho(\theta,\phi)\hat{v}(\theta,\phi) = \vec{V} - \vec{N}(\theta,\phi)\,, \tag{25}$$

where ρ is the distance from facet to satellite and $\hat{v}$ is the unit direction vector. Evaluating each term, we find

$$\rho(\theta,\phi) = \sqrt{(R_{\text{sat}} - R_E\cos\phi\sin\theta)^2 + R_E^2\sin^2\phi\sin^2\theta + R_E^2\cos^2\theta} \to R_{\text{sat}} \tag{26}$$

$$\hat{v}(\theta,\phi) = \frac{1}{\rho(\theta,\phi)}\,[R_{\text{sat}} - R_E\cos\phi\sin\theta \quad R_E\sin\phi\sin\theta \quad R_E\cos\theta]^\top \to [1 \;\; 0 \;\; 0]^\top\,. \tag{27}$$

Then the dot products in (14) may be expanded

$$\left(\hat{v}(\theta,\phi)\cdot\hat{N}(\theta,\phi)\right) \to \cos\phi\sin\theta \tag{28}$$

$$\left(\hat{L}\cdot\hat{N}(\theta,\phi)\right) \to \cos\phi\sin\theta\cos\alpha + \sin\phi\sin\theta\sin\alpha\,. \tag{29}$$

Putting it all together and rearranging terms, we find the flux-at-satellite integral expression in the large altitude limit resolves to

$$\tilde{F}_E \to \frac{R_E^2}{\pi R_{\text{sat}}^2}\int_{\alpha-\frac{\pi}{2}}^{\frac{\pi}{2}} \left(\cos^2\phi\cos\alpha + \cos\phi\sin\phi\sin\alpha\right)\,d\phi \int_0^{\pi}\sin^3\theta\,d\theta \tag{30}$$

$$= \frac{2R_E^2}{3\pi R_{\text{sat}}^2}\left[((\pi-\alpha)\cos\alpha + \sin\alpha\right]\,. \tag{31}$$

Et voilà, we have recovered (1) with $\Phi \equiv \alpha$. RSOs near GEO have $R_{\text{sat}} \approx 5.5\,R_E$; while this is not an enormous multiplicative scale, we see that perturbations to the diffuse sphere earthshine model are suppressed by a moderate factor for GEO RSOs, whereas the expansion breaks down in LEO where $R_{\text{sat}} < R_E$. In addition to prior research where this approximation has been successfully applied to GEO RSOs, we empirically observe the different levels of agreement in Fig. 8 as well.